ASEAN Engineering Journal

Full Paper

EXPERIMENTAL AND NUMERICAL INVESTIGATION ON THE EFFECT OF PCM AND EXTERNAL REFLECTORS ON THE PERFORMANCE OF A CONVENTIONAL SOLAR STILL

Omar Abd UL-Qader Mohammed, Ayser Muneer Flayh

Department of Mechanical Engineering, College of Engineering, University of Baghdad, Iraq

Article history
Received
05 September 2024
Received in revised form
23 April 2024
Accepted
15 June 2025

*Corresponding author
Omar.abd2103m@
coeng.uobagdad.edu.iq

Graphical abstract

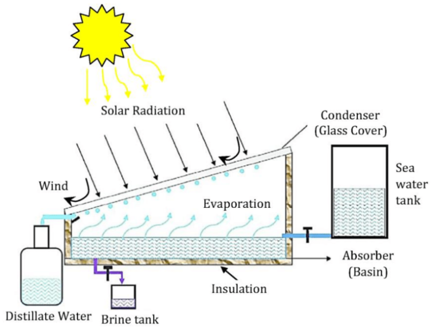

Abstract

The conventional solar still (CSS) is a device that utilises solar energy to generate distilled water by employing thermal processes such as evaporation and condensation of brackish water The CSS is a desalination system in the development stage; further enhancement is required to increase its output yield. In the current study, an experimental and numerical investigation was conducted to explore the impact of using PCM and external reflectors on the performance of conventional solar still during different months in the climate of Baghdad. Also, the impact of water depth was examined for 2 cm, 3 cm, and 4cm. Furthermore, a series of numerical simulations using ANSYS-FLUENT commercial software was conducted. The results showed that using PCM improves the yield by 8% on average while using both PCM and external reflectors improves the yield by 24%. The results also revealed that increasing the water depth from 2 cm to 4 cm reduces the yield by 16%. The numerical simulation revealed that the numerical and experimental yield are in good agreement, with less than 5% as a maximum deviation.

Keywords: conventional solar still, solar energy, phase change material, external reflectors, , evaporation and condensation

1.0 INTRODUCTION

Water is a vital element for all kinds of human life and is abundant in nature. Approximately 72% of the Earth's surface is covered by water, yet just 1% is accessible for direct use as a freshwater supply [1]. Consequently, the scarcity of potable water in numerous regions of the globe is a significant issue, primarily due to the rapid social development, environmental degradation, and steep increase in population growth. There is an insufficient supply of fresh water for approximately 41% of the global population who live in coastal regions despite the widespread availability of saline water [2]. Therefore, solar desalination may be a viable alternative for converting brackish water to pure water by utilizing naturally occurring solar radiation. One of the primary deficiencies of solar desalination systems is the intermittent availability of solar radiation, which is influenced by environmental conditions. This necessitates the development of modern techniques that can accumulate excess solar energy during peak hours and discharge it when the sun sets [3]. Several researches have been carried out to enhance the accessibility of clean water via the use of solar stills. These studies have explored various changes to solar stills, including the integration of fins [4], thermoelectric modules [5], wick materials [6], photocatalysts [7], parabolic reflectors [8], Fresnel lenses, and other techniques. Tubular solar stills [9-10], pyramid solar stills [11], stepped double slope solar stills [12], Weir-cascade solar stills [13], and pyramid stills with evacuated tubes [14] are several designs that have been developed to enhance the daily output of sun stills via various improvements. Thermal energy accumulation may be used as a method to decrease the discrepancy between available and needed energy sources. Energy may be stored in several ways, but the most efficient storage methods are via sensible or latent heat [15].The use of energy-storage materials, which may store either sensible or latent heat, into sun desalination systems enhances the efficiency of solar stills. Several studies have already been conducted using materials that can store heat in a sensible form, such as sandbags, pebbles, steel wool fibre, brick pieces, and quartzite. Systems utilizing latent heat have been found to have superior heat accumulation capabilities compared to sensible heat systems. This is due to their excellent energy storage capacity, continuous phase transition process, and the requirement of less energy material during the phase transition process [16-19]. The use of phase change material (PCM) to utilise latent heat has shown to be the most promising and dependable method for accumulating a significant amount of energy throughout the process of melting and freezing. Phase Change Material (PCM) in the solar system has the ability to store an excessive quantity of radiation from the sun during the hours when sunlight is at its height. This stored energy may be released as needed during periods of low sunlight, in both sensible and latent forms [20]. Suraparaju and Natarajan [21] investigated experimentally the performance of different designs of sola desalination systems, including single-slope conventional solar still (CSS), CSS with absorber plate finned with solid fins inserted in Parrafin wax and CSS with absorber plate finned with hollow fins inserted in Paraffin wax. The tests were conducted for tew consecutive days to ensure similar meteorological conditions. The results inferred that adding hollow fins yielded more than the solid fins due to a larger surface area in contact with the PCM. It was reported that using hollow fins and solid fins with the PCM augmented the productivity by 41% and 20%, respectively. Ghadamgahi et al. [22] experimentally investigated the effect of using a phase change material on the performance of a multi-stage solar still. The impact of using paraffin wax at the back of the absorber surface on productivity was investigated for 25mm and 50mm water depths. The results revealed that using paraffin wax with a thickness of 25 mm augments freshwater productivity by 15%. Also, it was found that increasing the paraffin thickness from 25mm to 50 mm decreases productivity by 36%. The maximum efficiency was reported at 38%, 32%, and 53% for the cases without pcm, with 50 mm thickness pcm and 25mm thickness pcm, respectively. Grewal et al. [23] experimentally investigated the influence of using a phase change material on the performance of a stepped solar still. Paraffin wax was loaded in metal tubes and fixed on the absorber plate. Also, the effect of preheating the feedwater using an evacuated tube collector was investigated. The results indicated that introducing the PCM tubes increases productivity of freshwater by 20% while using the evacuated tube preheater increases productivity by 30% compared to traditional stepped solar still. Integrating the paraffin wax tubes and the preheater into the solar still augmented the productivity by 98% and achieved a maximum efficiency of 46.9%. Also, the results indicated that using pcm increases the working time of the still by 3 hours. Cheng et al. [24] performed both experimental and theoretical research to examine the impact of utilizing shape-stabilized phase change material (SSPCM) as an absorber plate on the efficiency of a pyramid solar still. The SSPCM is composed of paraffin wax and 5% graphite. The experimental results indicated an enhancement of 43% in productivity when using SSPCM. The theoretical results revealed that increasing the thermal conductivity of the SSPCM from 0.2 W/m.K to 4 W/m.K augments the productivity by 75%. Also, it was found theoretically that increasing the melting point of the SSPCM from 34 ^{o}C to 50 ^{o}C improves the productivity by 3%. Mousa et al. [25] experimentally investigated the impact of using candle wax encapsulated in tubes as a PCM on the productivity of a single-slope solar still. The effect of the mass ratio of PCM to water was investigated in the range from 0 to 0.51. The results indicated that the relation between the productivity and the mass ratio of PCM to water is inversely proportional during the daytime and directly proportional during the nighttime. Increasing the mass ratio from 0 to 0.51 decreases the productivity during the day by 26% while increasing it in the nighttime by 100%. Rufuss et al. [26] tested a conventional still load with nanoparticle-enhanced Paraffin wax. Accordingly, four solar stills were examined: a conventional still (CSS), a CSS with paraffin enhanced with TiO_2, a CSS with paraffin enhanced with CuO, and a CSS enhanced with Graphene Oxide. The highest yield was obtained by the CSS with CuO nanoparticles. Essa et al. [27] investigated the impact of using paraffin wax PCM mix with Ag-Nano particles under the absorber surface on the productivity of a pyramid solar still. The absorber surface was pyramidal to increase the exposed surface area to the radiation and evaporation surface area. The experiment's results demonstrated that using PCM-Ag resulted in a 36% increase in the daily productivity of the pyramidal absorber PSS. Kumar et al. [28] experimentally investigated the performance of single-slope solar still using paraffin wax phase change material (PCM) and silica-paraffin nano phase change material (n-PCM). The results revealed 51.22% and 67% enhancements in productivity when using PCM and n-PCM, respectively.

Several authors investigated the performance of the conventional solar still numerically using CFD software. Saeed et al. [29] numerically investigated the impact of implementing a nano-PCM on the diurnal yield of a single-slope solar still. COMSOL software was implemented to test the impact of introducing a paraffin wax-Al_2O_3 nanoparticle mixture under the basin. It was reported that the daily yield was improved by 20% when using 1 kg of paraffin wax with a 3% volume concentration of Al_2O_3 nanoparticles. Hafs et al. [30] numerically modeled the combination of a phase change material with active and passive solar still using COMSOL software. The active still included the integration of a passive solar still with a parabolic trough collector (PTC) through a heat exchanger. Also, the effect of absorber design was tested, including flat, rectangular, triangular, and spherical shapes. The simulation results revealed that the passive still absorber with rectangular ripples augmented the productivity by 109% and 42% compared with conventional still and still with flat absorber and PCM. In addition, it was shown that when solar energy is combined with PTC and changed with various absorber geometries, it results in a much greater freshwater productivity. Specifically, the productivity is 549% higher compared to a passive still using rectangular absorbers, and 611% higher compared to a passive still using spherical absorbers. Moreno et al. [31] investigated numerically, using Ansys-Fluent, the influence of adding different PCMs, including RT45 HC, RT62 HC, RT70 HC, and RT80 HC, on the performance of a single-slope solar still. The results revealed an enhancement in productivity by 10.82%, 13.23, and 4.86% when adding RT80 HC, RT70 HC, and RT62 HC, respectively, while adding RT45 HC reduced the productivity by 2.95%. Furthermore, decreasing the thickness of RT70 HC from 10 mm to 2.5 mm improved the productivity by 5.6%. For the sun-off operation, it was indicated that the lower temperature PCM gave higher productivity. Rashid et al. [32] explored numerically the effect of Al_2O_3 – water nanofluid on the performance of conventional solar still. They revealed that using

Al_2O_3 – water nanofluid improves the evaporation and condensation inside the still. Also, they reported that increasing the volume fraction by from 0% to 5% augments the productivity by 25%.

Reviewing the literature reveals that no work incorporates conventional solar stills with PCM and external reflectors. Therefore, the present work presents an experimental investigation of the performance of a conventional solar still incorporated with PCM and external reflectors. Also, a numerical simulation using Ansys-Fluent explores the impact of water depth on the yield .

2.0 EXPERIMENTAL SETUP

The experimental setup of the present work was located at the College of Engineering, Baghdad University, Iraq (latitude 33.3152, longitude 44.361488). The experiments were conducted in February. Figures 1 and 2 show a photo and schematic of the experimental setup for the three investigated cases. The experimental setup consists of two identical single-slope solar stills. The basin area of each still is 1 m2 (1 m x 1 m). The low sidewall height is (250) mm, and the high side wall is (900) mm. The still is fabricated from galvanized steel sheets with (1) mm thickness. The surfaces of the basin are coated with black paint to improve the absorptivity. The bottom and sides of the still are insulated with a cork of (50) mm and plywood of (10) mm to minimize the heat loss from the still to the ambient. The glass cover is fabricated from transparent glass sheets (3) mm thick with an inclination angle (33°) horizontally, which is the latitude of Baghdad, Iraq [33]. The experimental setup is oriented in the south direction to receive the maximum solar radiation throughout the year. A small electric pump supplies saline water to the basin from a reservoir. An electric level controller controls the operation of the pump. The controller has three probes fixed inside the basin at the desired water level. Hiroshi [34] mentioned that the upper reflector can be tilted forward or backward by the changing seasons. During winter, the sun's altitude angle decreases, causing a significant portion of the reflected light from the vertical reflector to miss the still and reach the ground. Therefore, it is recommended to tilt the upper reflector slightly forward. Conversely, the altitude angle of the sun rises throughout the summer, making it difficult for the vertical reflector to redirect sunlight to the stationary position efficiently. Hence, it is recommended to have a modest backward tilt for the upper reflector, with an inclination angle of less than 25° consistently throughout the year. Tanaka [35] indicated that adding a flat bottom reflector to the still, which extends from the lower edge and slopes horizontally upwards, would enhance the absorption of solar radiation and raise the productivity of the distillate. So, in the present study (the experiments in the summer season), the angles of the top and bottom external reflectors were set at 15° and 50°, which was predicted as an optimum reflector angle in the summer season. The reflectors are fabricated from mirror steel of a thickness of 0.8 mm.

Paraffin wax is used as a thermal storage material and introduced below the basin bottom of the still. A holder basin holds 20 kg of paraffin wax between the water basin and the insulation. At first the PCM is melted and poured into the holder basin so it equally spread after solidification. After the PCM is solidified, the holder basin is assembled with the water basin and the insulation. The thermal properties of the paraffin wax are presented in Table 1. The thickness of the paraffin wax is 5 cm.

Table 1 Thermal properties of Paraffin wax.

Property	Value
Melting temperature	48 °C
Density of liquid/solid	830/930 kg/m^3
Latent heat of fusion	190000 J/kg
Thermal conductivity	0.21 W/m °C
Specific heat	2100 J/kg °C

Figure 1 Photo of the still

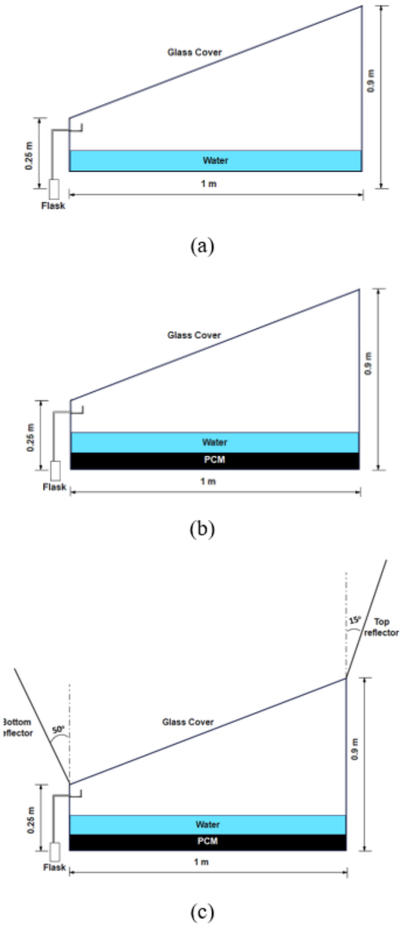

a) conventional solar still (CSS), b) CSS with PCM, c) CSS with PCM and reflectors

Figure 2 Schematic of the still

3.0 MEASUREMENTS AND UNCERTAINTY

Table 2 displays a comprehensive list of the measuring equipment together with their respective characteristics. The quantities being monitored are sun radiation, wind speed, and still temperatures. The measurement and recording of irradiance is done using a digital datalogger known as SPM 1116SD. The measurement of wind speed is obtained by utilizing a digital anemometer known as the UT361. A total of eighteen type-K thermocouples, which have been calibrated, are employed to accurately measure the temperatures of various components including glass, vapor, saline water basin walls, and paraffin wax. The thermocouples are placed in the following manner: three on the outer surface of the glass, two on the inner surface of the glass, two for the vapor, three inside the salty water, four on the side walls of the basin, and four within the paraffin wax. The thermocouples' readings are monitored and stored using a digital data recorder called Lutron BTM-4208. A flask with a volume of 250 ml is utilized to quantify the yield. The uncertainty is calculated using the nominal accuracy provided by the maker of the device. The estimation of standard uncertainties is obtained by dividing the correctness of the title by a factor of 1.7302 [36]. The cumulative uncertainties are computed using Equation (1) [37]. The uncertainties for standard and cumulative values used in this investigation are specified in Table 3.

$$u_R = \pm\sqrt{\left(\frac{\partial R}{\partial x_1}u_{x_1}\right)^2 + \left(\frac{\partial R}{\partial x_2}u_{x_2}\right)^2 + \cdots\cdots + \left(\frac{\partial R}{\partial x_n}u_{x_n}\right)^2} \qquad (1)$$

where $R = f(x_1, x_2, x_3 \ldots \ldots, x_n)$.

Table 2 Technical information of measurement devices

Parameter	Instrument	Model	Accuracy
Temperature	Thermocouple	K-Type	±1%
Solar radiance	Solar power meter	SPM 1116 SD	±5%
Water yield	Graduated cylinder	EISCO	1%
Wind speed	Anemometer	UT361	±3%

Table 3 Standard and accumulated uncertainties.

Parameter	R	S	u_x
Temperature	T	±1%	±1%
Solar radiance	I	±5%	±5%
Water yield	m_w	1%	1%
Wind speed	V	±3%	±3%

4.0 PERFORMANCE METRICS

The daily efficiency is calculated by summing the hourly condensate output m_w and multiplying it by the latent heat. so, the result is divided by the daily average solar radiation I (t)over the whole area [38]:

$$\eta_d = \frac{\sum_{i=1}^{24} m_w h_{fg}/3600}{\sum A\, I(t)} \qquad (2)$$

Where m_w is the mass of condensed water (kg), η_d is still efficiency, A is the basin area (m^2), I is the solar irradiation (W/m^2), h_{fg} is the latent heat of water vaporization (J/kg), it is calculated as:

$$h_{fg} = 10^3\left(2501.9 - 2.40706 \times Tw + 1.192217 \times 10^{-3}\, Tw2 - 1.5863 \times 10^{-5}\, Tw^3\right)$$

(3)

5.0 NUMERICAL SIMULATION

5.1 Physical Model

The physical model is a single-slope basin solar still whose bottom is 1m and whose height depends on the water depth with of inclination angle of 33°. Figure 3 illustrates the model dimensions for water depths 2 cm and 3 cm. The PCM is not directly involved in the model but its effect on temperature is involved.

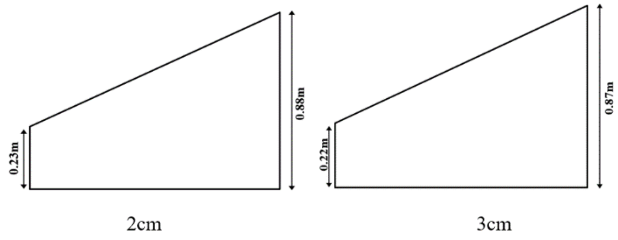

Figure 3 Schematic of the still models

5.2 Governing Equations

The following equations are used to simulate the fluid flow, heat transfer and mass transfer inside the still.

Continuity equation

$$\frac{\partial \rho}{\partial t} + \nabla.(\rho\vec{v}) = 0 \qquad (4)$$

Where

ρ : density (kg/m^3).

t : time (sec).

v : velocity (m/s).

Momentum equation

$$\frac{\partial}{\partial t}(\rho\vec{v}) + \nabla.(\rho\vec{v}\,\vec{v}) = \nabla P + \nabla.\left(\overrightarrow{\tau_{eff}}\right) + \rho\vec{g} \qquad (5)$$

Where

τ : stress tensor (N/m^2).

g : Gravitational acceleration (m/s^2).

Energy equation

Air water mixture

$$\frac{\partial}{\partial t}(\rho\,\overline{E}) + \nabla.\left(\vec{\overline{v}}(\rho\,\overline{E} + \,\overline{P})\right) = \nabla.\left(\lambda_{eff}\,\nabla\overline{T} - \textstyle\sum_j \overline{h}_{E,j}\vec{\overline{J}}_j\right) + S_h + \,S_L \qquad (6)$$

Water

$$\frac{\partial}{\partial t}(\rho E) + \nabla.\left(\vec{\overline{v}}(\rho\,\overline{E} + \,\overline{P})\right) = \nabla.(\lambda\,\nabla\mathrm{T}) + S_L \qquad (7)$$

Glass

$$\frac{\partial}{\partial t}(\rho E) = \nabla.(\lambda\,\nabla\mathrm{T}) + S_L \qquad (8)$$

Where

E : Energy (W/m^3).

λ_{eff} : The effective thermal conductivity (W/m. K).

$\overline{h}_{E,j}$: sensible enthalpy (J/kg K).

$\vec{J}_j$: diffusion flux of species *j* (kg/m^{2}s).

P : pressure (Pa).

S_h : radiant energy (W/m^3).

S_L refers to the latent heat of evaporation or condensation, which is included in the energy calculation as a sink or source term [31]. By including evaporation and condensation, the temperature distribution may be accurately accounted for without the need for multi-phase models. To address the problem, the existing model includes a coefficient α to precisely measure the fraction of heat that is either transferred from the water or transmitted to the glass. Equation (9) illustrates the computation of the sink/source term SL, which is influenced by α and the evaporation/condensation rate for each constituent of the solar still.

$$S_L = \begin{cases} +\dfrac{\alpha\dot{m}_c h_{fg,g} A_g}{V_g} & for\ glass \\ -\dfrac{\alpha\dot{m}_e h_{fg,w} A_w}{V_w} & for\ water \\ \dfrac{+(1-\alpha)\dot{m}_c h_{fg,g} A_g - (1-\alpha)\dot{m}_e h_{fg,w} A_w}{V_a} & for\ air\ water\ mixture \end{cases} \qquad (9)$$

Where

$\dot{m}_c$: condensation flux rate on the glass surface (kg/m^2.s).

$\dot{m}_e$: evaporation flux rate on the water surface (kg/m^2.s).

$h_{fg,g}$: enthalpy of condensation at glass temperature (J/kg K).

$h_{fg,w}$: evaporation enthalpy at water temperature (J/kg K).

A_g : surface area of glass cover (m^2).

A_w : surface area of water (m^2).

V_g : volume of glass (m^3).

V_w : volume of water (m^3).

V_a : volume of air (m^3).

Fick's law is implemented to express the rate of condensation and evaporation as in eqs (10) and (11). The rates are integrated on glass and water surfaces to obtain the total evaporation and condensation rate at each time step.

$$\dot{m}_c = \frac{-\rho D_m}{L_g}\int_0^{L_g}\frac{\partial C}{\partial \acute{y}}\bigg|_{glass} d\acute{x} \qquad (10)$$

$$\dot{m}_e = \frac{-\rho D_m}{L_w}\int_0^{L_w}\frac{\partial C}{\partial y}\bigg|_{water} dx \qquad (11)$$

Where

L_g : glass cover length (m).

L_w : water length (m).

y : vertical coordinate perpendicular to the water surface.

$\acute{y}$: vertical coordinate perpendicular to the glass surface.

where D_m is the molecular diffusion coefficient of water vapor in the air and taken as 2.88e-05 m^2/s.

Figure 4 shows the coordinates for the glass and water surfaces and the length of the glass and water surfaces.

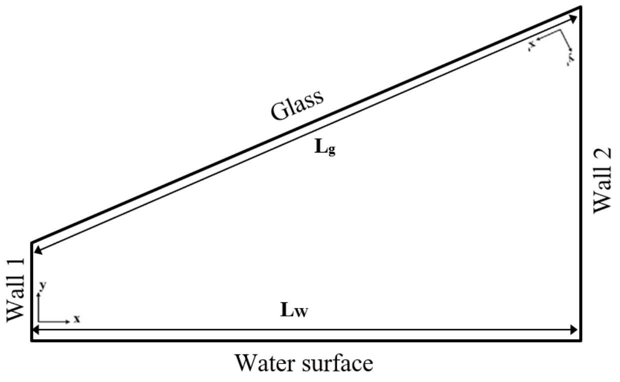

Figure 4 Physical model with coordinates.

Species transport

The water vapor concentration in the humid air at each location in the domain is determined by solving the species dispersion equation [39].

$$\frac{\partial}{\partial t}(\rho\bar{C_i}) + \nabla.\left(\vec{\overline{v}}\,\bar{C_i}\right) = \nabla.\vec{J_i} \qquad (12)$$

C: is the mass fraction of a species

J_i represents the diffusion flow of species i, which occurs as a result of concentration and temperature gradients. ANSYS FLUENT employs Fick's law as the default method for modeling mass diffusion caused by concentration gradients. According to this law, the diffusion flux may be expressed as:

$$\vec{J_i} = -\rho D_{i,m}\,\nabla C_i - D_{i,T}\frac{\nabla\mathrm{T}}{T} \qquad (13)$$

Where $D_{i,T}$ is the thermal diffusion coefficient?

The hourly produced fresh water is determined by the integration of Eq. (14) for every hour.

$$\dot{m}_c = \frac{-3600\times\rho D_m}{L_g}\int_0^{L_g}\frac{\partial C}{\partial \acute{y}}\bigg|_{glass} d\acute{x} \qquad (14)$$

The mathematical model was developed with respect for the following:

- Since the pressure inside the still is low [31], air and water vapour are regarded as perfect gases.
- The interfaces between glass-air and air-water are fully saturated, meaning that the humidity ratio is at 100% [40].
- The impact of PCM on the temperature distribution is being considered rather than simulating the PCM itself.
- The water depth inside the still is constant along the day.
- The heat of condensation/evaporation is introduced into the system through a source term that is determined by the mass fluxes.
- The mass fraction of H_2O at the water and glass surfaces is computed on the assumption that they are fully saturated.

5.3 Boundary Conditions

At the start of the simulation, the entire system is assumed to have the same temperature. The initial temperature provided represents the ambient temperature at 8 AM, which marks the start of the simulation. Furthermore, there is an absence of movement and the proportion of water vapor, for all constituents in the air-water vapor mixture, is designated as zero. Table 4 outlines the boundary conditions used in the solution of the numerical model. The temperature used as boundary conditions are the temperatures from the experimental measurement.

Table 4 Standard and accumulated uncertainties.

Parameter	Instrument	Model	Accuracy
Glass	No slip	Variable Temp.	Cw=1
Water surface	No slip	Variable Temp.	Cw =1
Wall 1	No slip	Variable Temp.	-------
Wall 2	No slip	Variable Temp.	-------

5.4 Mesh Creation

A mesh independence analysis was conducted to determine the appropriate mesh for the simulations. Figure 5 shows the computational mesh with focusing on the inflation zones. In order to correctly capture the effect of the wall on the flow, simulations were executed to determine the appropriate number of mesh elements. Table 5 presents the independency test for the mesh for CSS with 2 cm water depth on 29th August 2023. The smaller the size of the mesh, the better the agreement between the experimental and numerical yield. Increasing the element number beyond 96,101 has an insignificant effect on the deviation; therefore, the element size 0.0025 m^3 corresponding to the element number 96,101 is selected as the meshing size for all simulations.

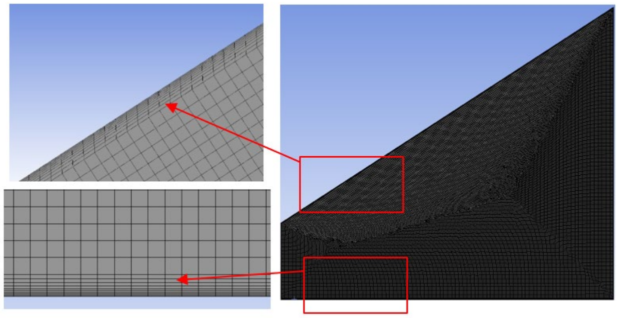

Figure 5 Computational mesh

Table 5 Mesh Independency Test

Trials	Elements no.	Exp. Yield (litre)	Num.Yield (litre)	Deviation
1	50,440	4.77	4.32	10%
2	63,586	4.77	4.38	8.1%
3	72,256	4.77	4.41	7.5%
4	82,452	4.77	4.46	6.5%
5	88452	4.77	4.49	5.8%
6	91256	4.77	4.52	5.2%
7	96101	4.77	4.59	3.6%
8	100,214	4.77	4.59	3.6%
9	102,451	4.77	4.59	3.6%

5.5 Thermophysical Properties

The ideal gas law is used to determine the density change of air and water vapor. All other thermophysical properties are assumed to be constant as presented in Table 6. The mixture was considered to be a combination of ideal gases due to the low pressure of the system. Thus, the density is determined by considering the volume of each species, whereas the other parameters are estimated using the mass-weighted mixture law.

Table 6 Thermophysical properties

Material	Density (kg/m^3)	Heat capacity (J/kg K)	Viscosity (kg/m s)	Thermal conductivity (W/m K)
Air	Ideal gas	1006.43	1.789e-5	0.028
Water vapor	Ideal gas	2014	1.34e-5	0.0261
Glass	2700	840		0.6

5.6 Solution

Numerical results were obtained using the finite volume method to solve the governing equations, assuming laminar flow. The SIMPLE technique was utilized to establish a connection between the momentum and continuity equations. The convective terms were discretized using second-order methods. The convergence of each time step was assessed by utilizing the weighted residue as the criterion.. The energy equation reached convergence with a value less than 10^$^{-6}$, whereas the other equations obtained convergence with a value less than 10^$^{-4}$. The time step size is set to 4 seconds with 25 iterations per time step.

6.0 RESULTS

6.1 Experimental Results

The experimental results were collected in Baghdad (33.27° N, 44.37° E) for three solar still configurations during February, August, and October. The first configuration is a conventional solar still (CSS). The second is a conventional solar still loaded with phase change material (CSS-PCM). The third is a conventional solar still with phase change material and external reflectors (CSS-PCM-R).

6.1.1 Conventional Solar Still (CSS)

A set of experiments was conducted on the 29th, 30th, and 31st of August 2023 under Baghdad clear sky to assess the impact of water depth on the performance of the conventional solar still. Figures 6, 7, and 8 illustrate the measured temperatures of basin, water, vapor, and glass along with weather conditions of solar radiation and ambient temperature for water depths of

2cm, 3cm, and 4 cm, respectively. The maximum solar intensities for the three consecutive days are 826 W/m^{2}, 810 W/m^{2,} and 809 W/m^{2,} while the average intensities are 567 W/m^{2}, 550 W/m^{2,} and 544 W/m^{2}. The maximum ambient temperatures for the three consecutive days are 37 ^{o}C, 38 ^{o}C, and 37 ^{o}C, while the average ambient temperatures are 34 ^{o}C, 36 ^{o}C, and 35 ^{o}C. For a water depth of 2 cm, the maximum temperatures of the basin, water, vapor, and glass are 72 ^{o}C, 67 ^{o}C, 58 ^{o}C, and 56 ^{o}C, respectively. The average temperatures of the basin, water, vapor, and glass are 62 ^{o}C, 58 ^{o}C, 50 ^{o}C, and 48 ^{o}C, respectively. For a water depth of 3 cm, the maximum temperatures of the basin, water, vapor, and glass are 70 ^{o}C, 66 ^{o}C, 57 ^{o}C, and 55 ^{o}C, respectively. The average temperatures of the basin, water, vapor, and glass are 60 ^{o}C, 57 ^{o}C, 50 ^{o}C, and 47 ^{o}C, respectively. For a water depth of 4 cm, the maximum temperatures of the basin, water, vapor, and glass are 68 ^{o}C, 64 ^{o}C, 55 ^{o}C, and 53 ^{o}C, respectively. The average temperatures of the basin, water, vapor, and glass are 59 ^{o}C, 55 ^{o}C, 48 ^{o}C, and 45 ^{o}C, respectively. Figures 9 and 10 depict the effect of water depth on the water and glass temperature of the CSS. The temperature distribution follows the solar radiation curve. The temperatures inside the CSS decrease as the saline water depth increases due to the increased water content inside the basin, which absorbs more heat.

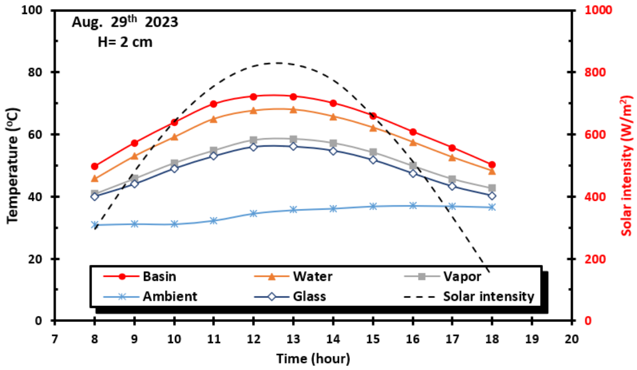

Figure 6 CSS basin, water, vapor, glass temperatures, and weather conditions (H=2 cm).

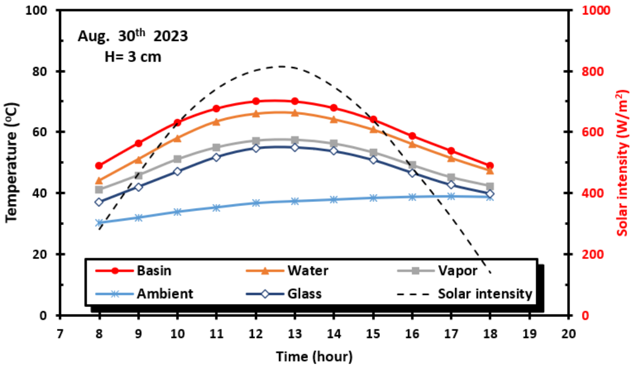

Figure 7 CSS basin, water, vapor, glass temperatures, and weather conditions (H=3 cm).

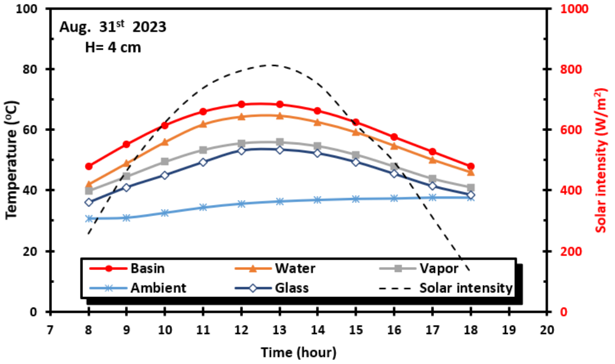

Figure 8 CSS basin, water, vapor, glass temperatures, and weather conditions (H=3 cm).

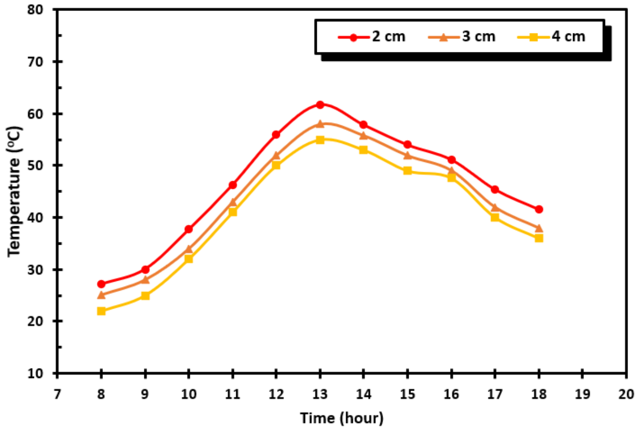

Figure 9 Water temperature of CSS for different water depths (20th, 21st, and 22nd October. 2023).

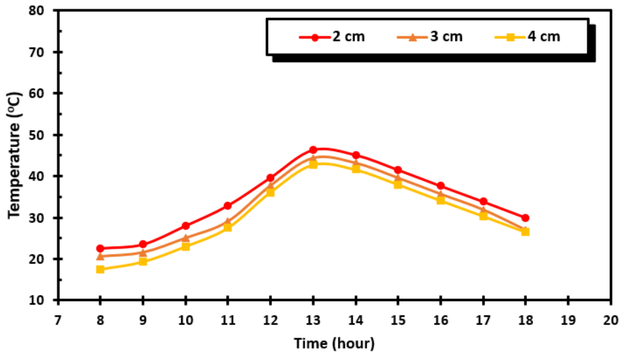

Figure 10 Glass temperature of CSS for different water depths (20th, 21st, and 22nd October. 2023).

Figure 11 shows the hourly solar intensity and yield of distilled water for the three water depths for the CSS on the 29th, 30th, and 31st of August. The still is initially filled with 20 litres, 30 litres, and 40 litres for saline water depths of 2 cm, 3 cm, and 4 cm, respectively. The water content is kept constant during the experiment. It is evident that the hourly yield gradually rises from sunrise and reaches its maximum value at midday, after which it declines in accordance with the dispersion of solar radiation. The CSS yield between 8:00 am and 9:00 am was 0.14

litre, 0.134 litre, and 0.126 litres for water depths of 2 cm, 3 cm, and 4 cm, respectively, and rises following the solar intensity distribution to achieve the peak value of 0.73 litres, 0.64 litres, and 0.59 litre at 1 pm and then the declines following the solar radiation distribution.

Figure 12 displays the total amount of freshwater produced by the CSS. The total amount of liquid collected between 8:00 am and 6:00 pm is 4.77 liters, 4.29 liters, and 3.98 liters for water depths of 2 cm, 3 cm, and 4 cm, respectively. The cumulative yield exhibited a 10% decline when the water level increased by 50% and a 16.5% decrease when the water depth increased by 100%. This behavior may be explained by the fact that as the water depth increases the amount of water in the still also increases from 20 kg to 30 kg and 40 kg. This increase in water quantity demands more thermal energy, which in turn leads to a decrease in the amount of distilled water produced.
Figure 14 shows the hourly solar intensity and yield of distilled water for the three water depths for the CSS on the 29th, 30th, and 31st of September. The CSS yield between 8:00 am and 9:00 am was 0.029 liter, 0.026 liters, and 0.022 liters for water depths of 2 cm, 3 cm, and 4 cm, respectively, and rises following the solar intensity distribution to achieve the peak value of 0.62 liter, 0.52 liter, and 0.4 liters at 13 pm and then the declines following the solar radiation distribution.

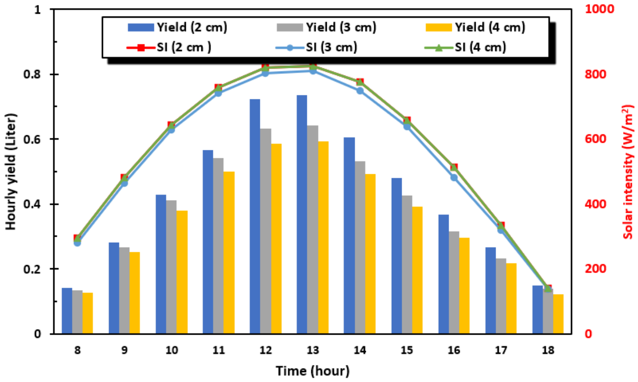

Figure 11 Hourly yield of distilled water of CSS (29th, 30th, and 31st Aug. 2023).

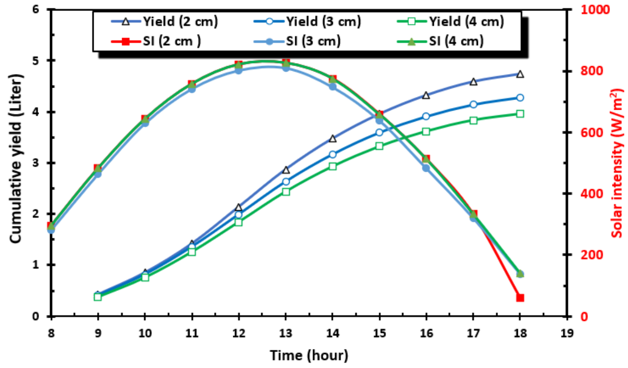

Figure 12 Cumulative yield of distilled water of CSS (29th, 30th, and 31st Aug. 2023).

The hourly and average thermal efficiency of the CSS for the different water depths 2 cm, 3 cm, and 4 cm on the 29th, 30th, and 31st of August are shown in figures 13 and 14. Generally, the efficiency increases from the sun shine to reach its peak at noon and decreases gradually following solar radiation intensity. The average efficiency is reduced by 8%, 16%, and 34% as the saline water depth increased by 50% and 100% for the test during August while decreasing by 9% and 18% for the tests during September. As the water depth increases, the efficiency decreases due to the lower yield caused by the larger water quantity inside the still, which requires more heat.

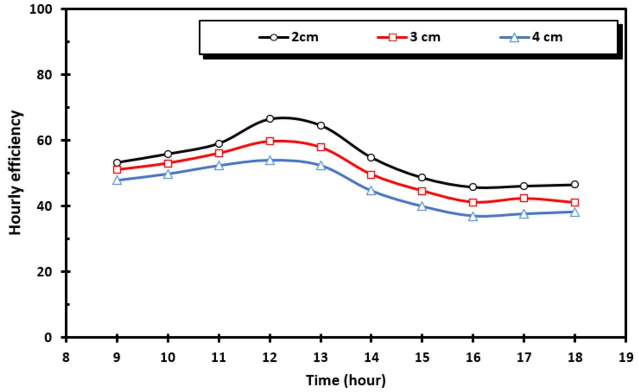

Figure 13 Hourly efficiency of CSS (29th, 30th, and 31st of August).

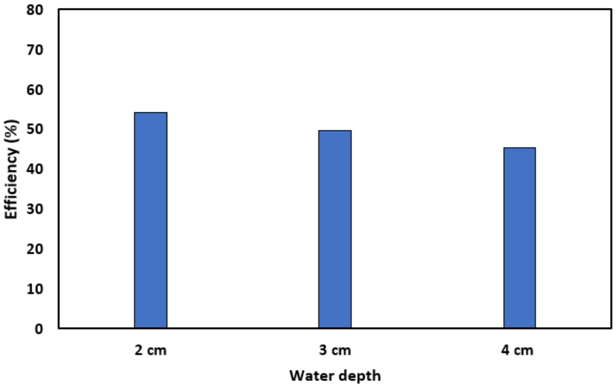

Figure 14 Hourly efficiency of CSS (29th, 30th, and 31st of August).

6.1.2 Conventional Solar Still with Phase Change Material (CSS-PCM)

The hourly and average thermal efficiency of the CSS for the Baghdad sky to determine the effect of water depth on the performance of the conventional solar still in the presence of Paraffin wax as a phase change material. Figures 15, 16, and 17 show the measured temperatures of the basin, water, vapor, glass, and PCM, along with weather conditions of solar radiation and ambient temperature for water depths of 2 cm, 3 cm, and 4 cm, respectively. The maximum solar intensities for the three consecutive days are 826 W/m^2, 810 W/m^2, and 809 W/m^2, while the average intensities are 567 W/m^2, 550 W/m^2, and 544 W/m^2. The maximum ambient temperatures for the three consecutive days are 37 °C, 38 °C, and 37 °C, while the average ambient temperatures are 34 °C, 36 °C, and 35 °C. For a water depth of 2 cm, the maximum temperatures of the basin, water, vapor, glass, and PCM are 70 ºC, 67 ºC, 57 ºC, 55 ºC, and 72 ºC, respectively. The average temperatures of the basin, water, vapor, glass, and PCM are 58 ºC, 55 ºC, 49 ºC, 46 ºC, and 60 ºC, respectively. For a water depth of 3 cm, the maximum temperatures of the basin, water, vapor, glass, and PCM are 68 ºC, 64 ºC, 55 ºC, 53 ºC, and 70 ºC, respectively. The average temperatures of the basin, water, vapor, glass, and PCM are 55 ºC, 51 ºC, 45 ºC, 42, and 57 ºC, respectively. For a water depth of 4 cm, the maximum temperatures of the basin, water, vapor, glass, and PCM are 67 ºC, 63 ºC, 53 ºC, 68ºC, and 68 ºC, respectively. The average temperatures of the basin, water, vapor, glass, and PCM are 54 ºC, 51 ºC, 43 ºC, 40 ºC, and 55 ºC, respectively. Figures 18, 19, and 20 present a comparison between the water temperatures of CSS and CSS-PCM for water depths 2 cm, 3 cm, and 4 cm, respectively. The water temperature for both CSS and CSS-PCM exhibits a similar behaviour during the charging time (nearly before 2:00 pm) with lower values of CSS-PCM. After the discharging initiates (nearly after 2:00 pm), the temperatures rise significantly due to the additional heat discharged from the Paraffin wax. The temperatures of CSS are lower than those of CSS-PCM, which is lower during the charging period because the PCM absorbs a significant amount of heat from the basin. Afterwards, during the discharging period, the process is inversed, and the heat released back from the PCM to the basin causes a significant rise. Also, it can be noticed that the effect of PCM on water temperature is more significant when the water depth is 2 cm, and it becomes less significant with the increase in water depth. This is because the larger quantity of water requires more significant heat to heat up.

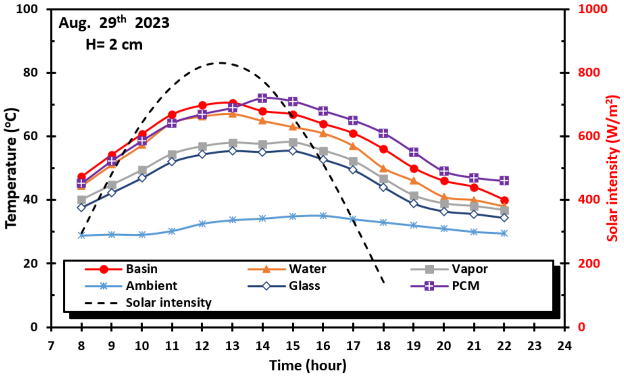

Figure 15 CSS-PCM basin, water, vapor, glass, PCM temperatures, and weather conditions.

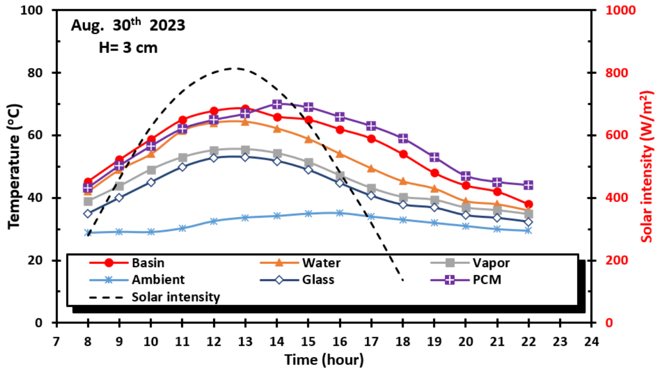

Figure 16 CSS-PCM basin, water, vapor, glass, PCM temperatures, and weather conditions.

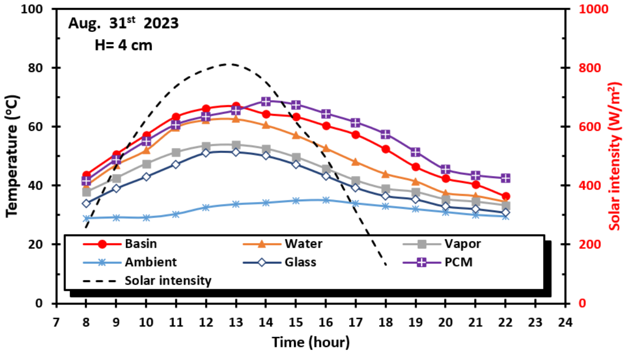

Figure 17 CSS-PCM basin, water, vapor, glass, PCM temperatures, and weather conditions.

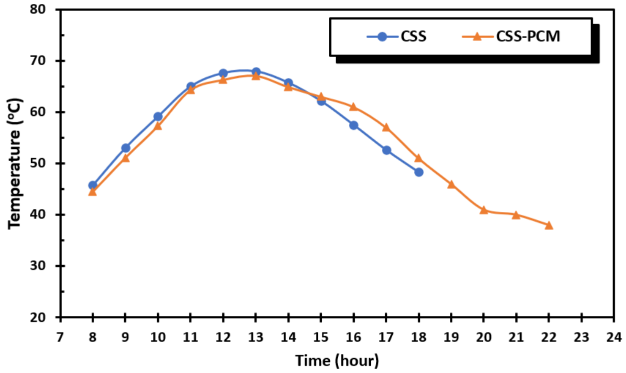

Figure 18 Water temperature of CSS and CSS-PCM for water depth H=2 cm (20th August. 2023).

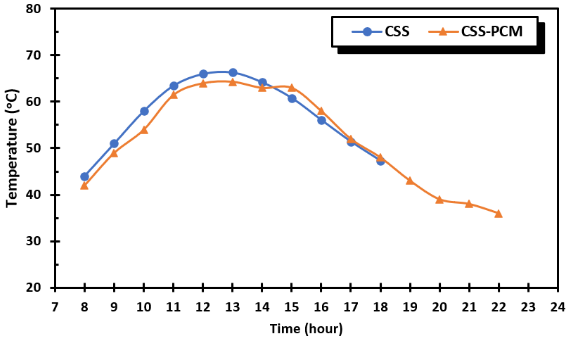

Figure 19 Water temperature of CSS and CSS-PCM for water depth H=3 cm (20th August. 2023).

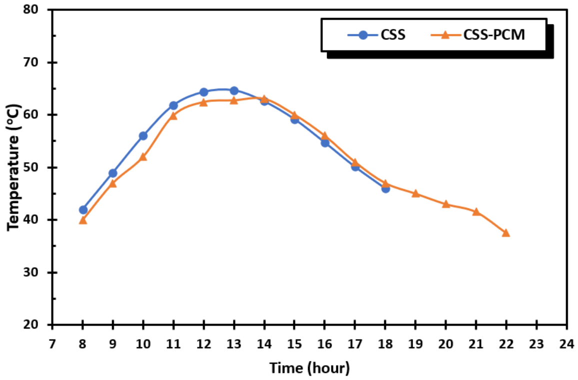

Figure 20 Water temperature of CSS and CSS-PCM for water depth H=4 cm (20th August. 2023).

Figure 21 shows the hourly solar intensity and yield of distilled water for the three water depths for the CSS-PCM on the 29th, 30th, and 31st of August. The still is initially filled with 20 liters, 30 liters, and 40 liters for saline water depths of 2 cm, 3 cm, and 4 cm, respectively. The hourly production has a noticeable pattern of increasing from dawn to its maximum value at midday, and thereafter decreasing gradually until midnight, in accordance with the dispersion of solar energy. Compared to the hourly yield distribution of CSS, the hourly yield after noon doesn't follow the solar radiation intensity behaviour but is strongly affected by the heat added by the PCM during the discharging period. The peak yield of CSS-PCM is 0.68 Liter, 0.64 Liter, and 0.6 Liter for water depths 2 cm, 3 cm, and 4 cm, respectively. As compared with the peak yield of CSS, the peak yield of CSS-PCM is lower than that of CSS by 12%, 3%, and 5% for the mentioned water depths. Also, it can be seen that using PCM extends the operation time of the CSS by four hours. Figure 22 depicts the cumulative yield of the CSS-PCM on the mentioned test days during August and October for the three water depths, along with solar intensity. The CSS-PCM yield between 8:00 am and 10:00 pm am is 5.05 liters, 4.64 liters, and 4.28 liters for water depths of 2 cm, 3 cm, and 4 cm, respectively.

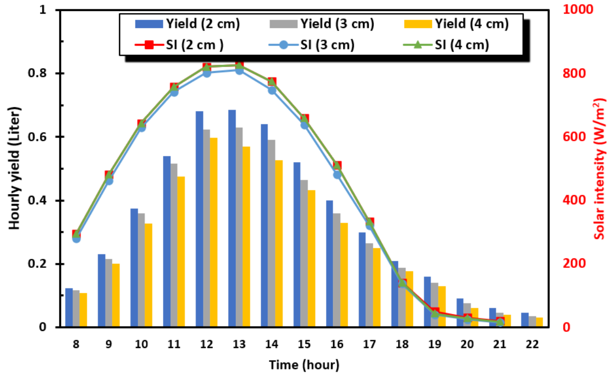

Figure 21 Hourly yield of distilled water of CSS-PCM (29th, 30th, and 31st Aug. 2023).

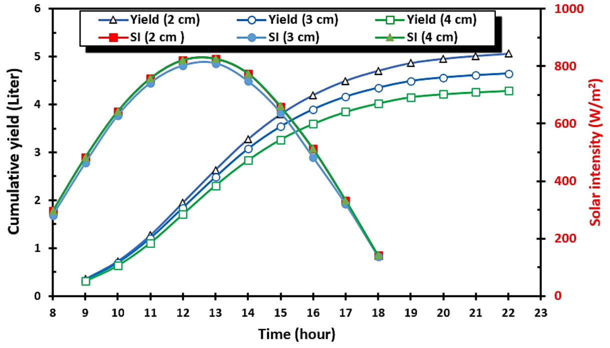

Figure 22 Cumulative yield of distilled water of CSS-PCM (29th, 30th, and 31st Aug. 2023).

Figures 23 compares the yield of the CSS and CSS-PCM for water depths 2 cm, 3 cm, and 4cm on the test days during August and October, respectively. Using PCM augments the yield of the CSS significantly due to the additional amount of heat added to the water by the PCM. The PCM increased the yield of the CSS by (6-8)% .

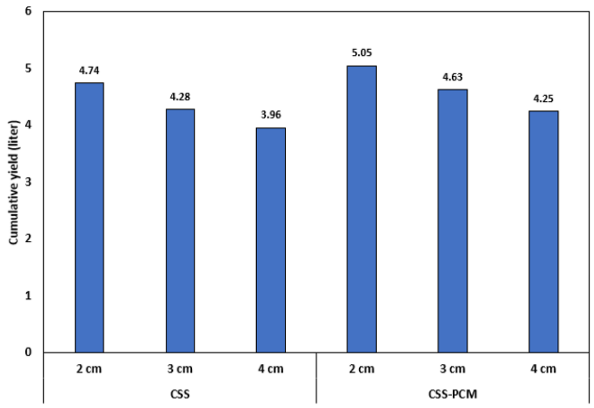

Figure 23 Comparison of the cumulative yield of distilled water of CSS and CSS-PCM (29th, 30th, and 31st August 2023).

Figures 24 shows the hourly efficiency of the CSS-PCM for different water depths on the 29th, 30th, and 31st of August. Generally, the efficiency increases from the sunshine to reach its peak at midnight. Compared to the hourly efficiency of CSS, the efficiency of CSS-PCM doesn't decline after noon and keeps rising due to the heat added by the PCM during the discharging period. Figures 25 compare the average efficiency of CSS and CSS-PCM for water depths 2 cm, 3 cm, and 4 cm on the test days during August. It was found that adding PCM into the CSS augments the efficiency by 7.5%, 9.2%, and 11% for water depths 2 cm, 3 cm, and 4 cm, respectively. Although the PCM decreases the yield before the noun, it augments the average efficiency significantly due to the increased hourly yield after noon during the discharging period.

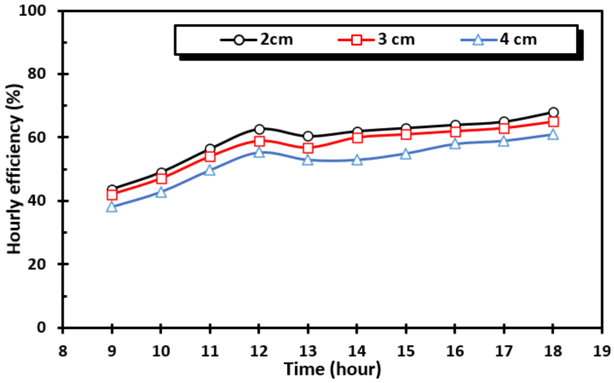

Figure 24 Hourly efficiency of CSS-PCM (29th, 30th, and 31st of August).

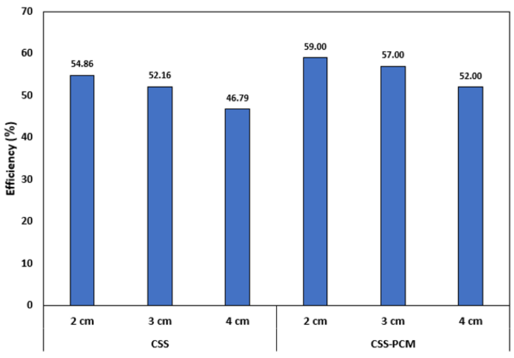

Figure 25 Average efficiency of CSS-PCM (29th, 30th, and 31st of August).

6.1.3 Conventional Solar Still with Phase Change Material with External Reflectors (CSS-PCM-R)

Another set of experiments was conducted in February 2024 to investigate the effect of external reflectors on the yield of the CSS-PCM. Figure 26 compares the yield of CSS, CSS-PCM, and CSS-PCM-R for water depths 2 cm and 3 cm for the test days 27, 28, and 29 February 2024. The figure indicates that using PCM increases the yield of the CSS by 0.25 litre and 0.13 litre for water depths 2 cm and 3 cm, respectively, while adding external reflectors to the CSS-PCM increases the yield by 0.45 litre and 0.27 litre for water depths 2 cm and 3 cm respectively. Also, Figure 27 shows the enhancement ratio of the external reflector and PCM on the still yield. Using PCM enhances the yield of the CSS by 8.6 % and 6% for water depths of 2 cm and 3 cm, respectively. Adding external reflectors augments the yield of the CSS-PCM by 14 % and 12 % for water depths of 2 cm and 3 cm, respectively. In other word, the effect of external reflectors on the yield is (12-14) %.

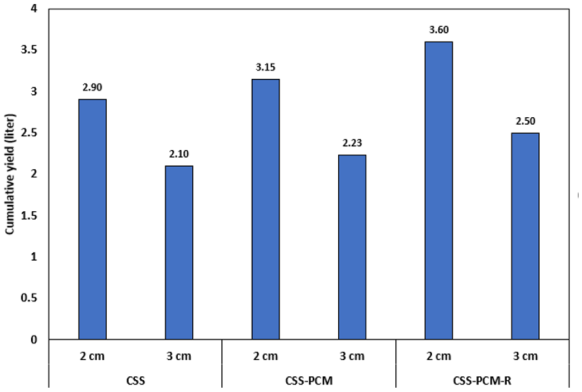

Figure 26 Comparison of the cumulative yield of distilled water of CSS, CSS-PCM, and CSS-PCM-R (27th, 28th, and 29th February 2024).

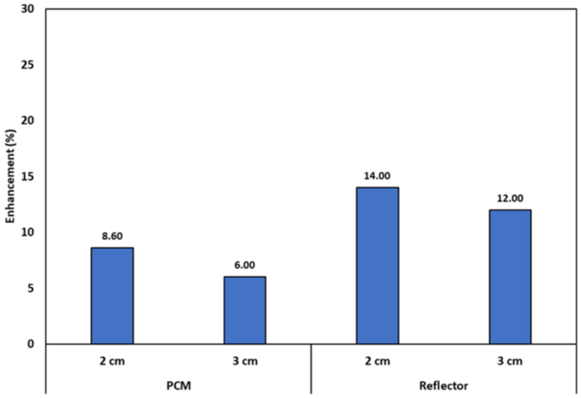

Figure 27 Enhancement ratio of using PCM and reflectors as compared to CSS (27th, 28th, and 29th February 2024).

6.2 Numerical Results

The numerical simulations were conducted only for CSS and CSS-PCM at water depths of 2 cm and 3 cm on the test days 29th and 30th August 2023. The temperature contours of the CSS at different hours (8,12,15,18) for water depths of 2 cm and 3 cm are displayed in Figure 28 for the test days 29th and 30th August 2023. At the beginning of the day, at 8 am, the temperature in the zone between the glass and the basin is the lowest while the temperature of the glass is higher and the temperature of the basin is the highest. As time passes, the temperature grades from the highest value at the basin to the lowest value at the glass. The temperatures inside the CSS at the different hours are higher for the water depth of 2cm. The maximum temperature for a water depth of 2 cm is higher by 3 °C than that of a water depth of 3 cm. Figure 29 depicts the temperature contours of the CSS-PCM at different hours (8,12,15,18,20,22) for water depths of 2 cm and 3cm. At the beginning of the day, a cold zone exists between the basin and the glass. After that, the temperature distributes gradually, so the higher temperature is at the basin, and the lower temperature is at the glass. The maximum temperature for CSS with a water depth of 2 cm is higher than that of 3 cm by (2-4) °C. Comparing the figures (5.44) and (5.45) reveals that the temperature inside the CSS-PCM is lower than that of the CSS by (2-3) °C.

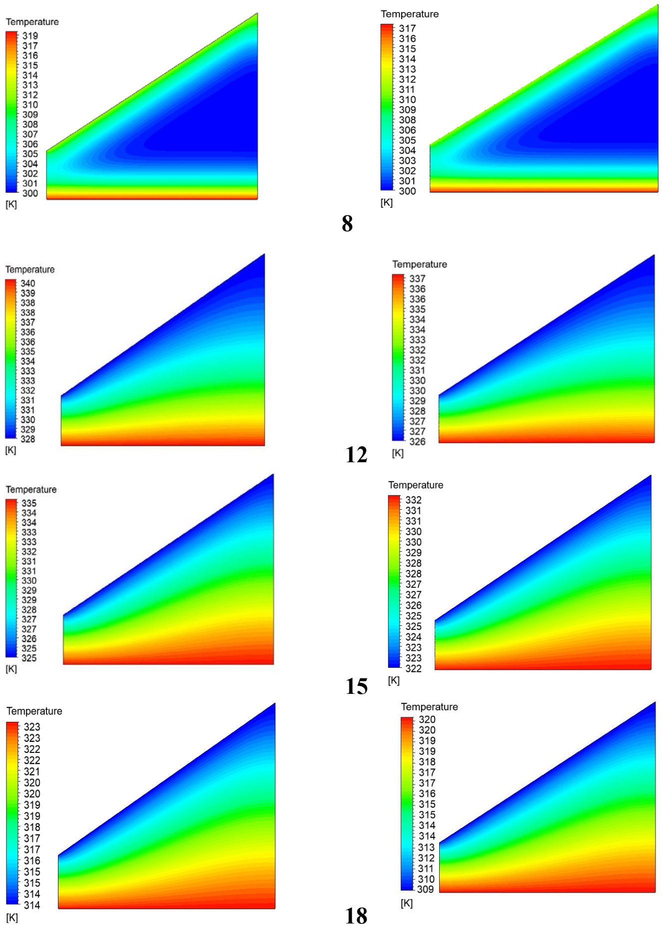

Figure 28 Temperature contours of CSS (29th and 30th August 2023).

A comparison of the experimental and numerical hourly yield of CSS for water depths 2 cm and 3 cm is depicted in figures 30 and 31 for the test days, 29th and 30th of August 2023. The hourly yield exhibits a good agreement between the experimental and numerical results. A deviation is noticed within the period between 11 am and 2 pm. This deviation is attributed to the complex nature of the flow and heat transfer inside the still. The deviation between the peak yield from numerical and experimental results is 17% and 12 % for water depths 2 cm and 3 cm, respectively. Figures 32 and 33 compare the experimental and numerical accumulative yield of the CSS-PCM for water depths 2 cm and 3cm, respectively, for the test day on the 29th and 30th of August 2023. The deviation between the peak value from experimental and numerical results is 18% and 12% for water depths 2 cm and 3cm, respectively. Figures 34 and 35 compare the cumulative yield from experimental and numerical results of CSS for water depths of 2 cm and 3 cm, respectively, for the same test days. The experimental and numerical accumulative yields are in excellent agreement, and the deviation is 3.7% and 2.2% for water depths of 2 cm and 3 cm, respectively. Figures 36 and 37 illustrate the experimental and numerical accumulative yield for CSS-PCM for 2cm and 3cm water depths, respectively, for the mentioned test days. The deviation between the numerical and experimental accumulative yield is 2.3% and 4.7% for water depths 2cm and 3cm, respectively.

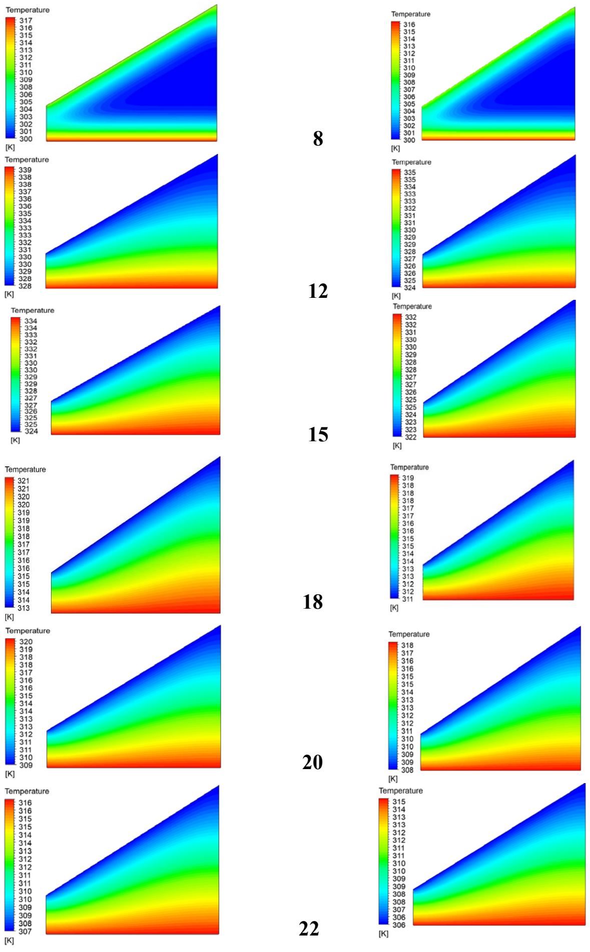

Figure 29 Temperature contours of CSS-PCM (29th and 30th August 2023).

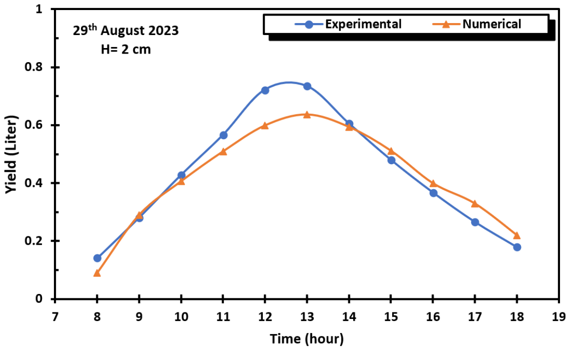

Figure 30 Experimental and numerical yield of CSS

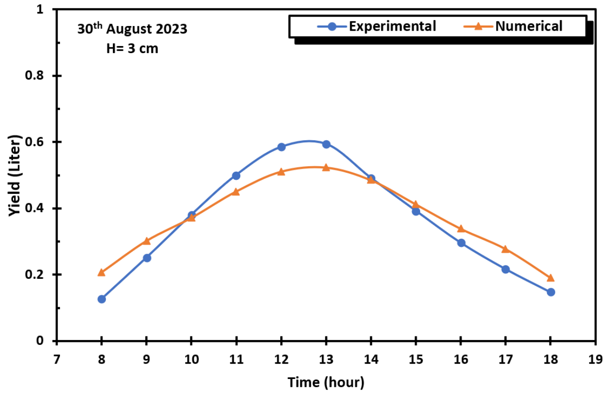

Figure 31 Experimental and numerical yield of CSS

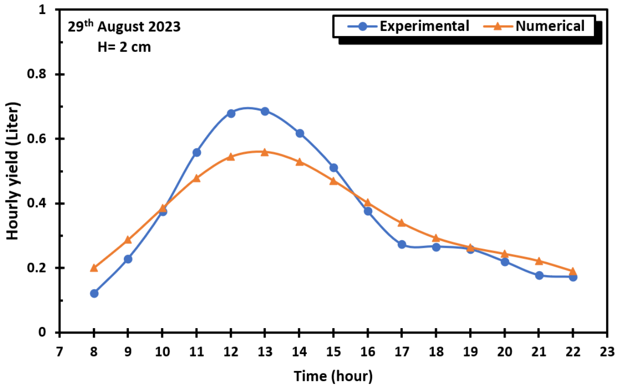

Figure 32 Experimental and numerical yield of CSS-PCM

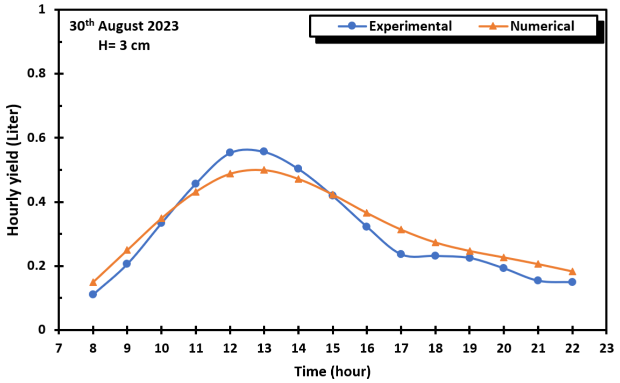

Figure 33 Experimental and numerical yield of CSS-PCM

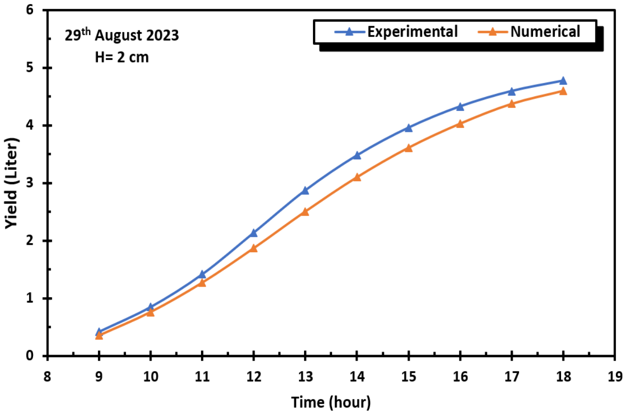

Figure 34 Experimental and numerical cumulative yield of CSS

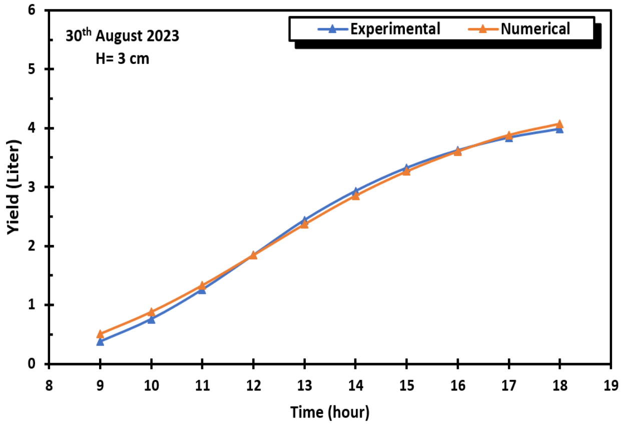

Figure 35 Experimental and numerical cumulative yield of CSS

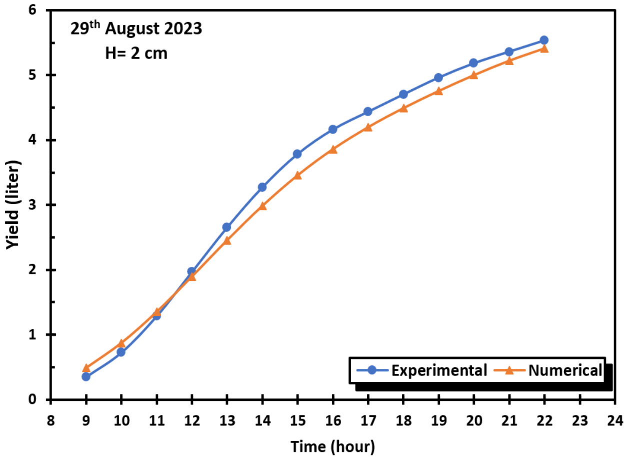

Figure 36 Experimental and numerical cumulative yield of CSS-PCM

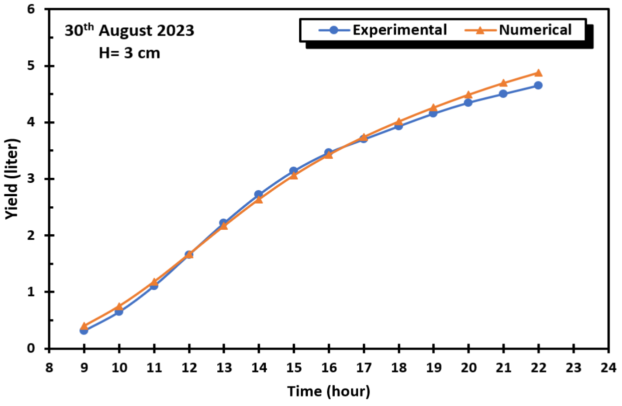

Figure 37 Experimental and numerical cumulative yield of CSS-PCM

7.0 CONCLUSIONS

In the present investigation, the effect of adding PCM and external reflectors on the performance of a conventional solar still is experimentally studied. Also, the effect of water depth was examined. The effect of adding PCM and water depth was also numerically investigated. The main conclusions can be summarized as follows:

- Increasing the water depth inside the still from 2 cm to 4 cm reduces the yield of CSS and CSS-PCM by 16%.
- The PCM increased the yield of the CSS by (6-8)% during August and by (8-29)% during October.
- Using external reflectors augments the yield by 14 % and 12 % for 2 cm and 3 cm water depths, respectively.
- Adding PCM extends the operation of the still for four hours.
- The numerical and experimental yield exhibits a high level of consistency, with a maximum discrepancy of less than 5%.

Acknowledgments

The authors would like to express their sincere appreciation to the College of Engineering, University of Baghdad, Iraq, for their continuous support and valuable contributions to this work

Conflicts of Interest

The author(s) declare(s) that there is no conflict of interest regarding the publication of this paper

References

[1] El-Sebaey, M. S., Ellman, A., Hegazy, A., & Ghonim, T. 2020. Experimental Analysis and CFD Modeling for Conventional Basin-Type Solar Still. *Energies*, *13*(21): 5734. DOI: https://doi.org/10.3390/en13215734

[2] Dixit, P., Vennapusa, J. R., Parvate, S., Singh, J., Dasari, A., & Chattopadhyay, S. 2021. Thermal Buffering Performance of a Propyl Palmitate/Expanded Perlite-Based Form-Stable Composite: Experiment and Numerical Modeling in a Building Model. *Energy & Fuels*, *35*(3): 2704–2716. DOI: https://doi.org/10.1021/acs.energyfuels.0c03553

[3] Han, X., Zhang, X., Hua, W., Yuan, W., Jia, X., & Wang, Z. F. 2019. Preparation and application of composite EG/Ba (OH)2 ·8H2 O form-stable phase change material for solar thermal storage. *International Journal of Energy Research*, *43*(6): 2227–2240. DOI: https://doi.org/10.1002/er.4438

[4] Velmurugan, V., Gopalakrishnan, M., Raghu, R., & Srithar, K. 2008. Single basin solar still with fin for enhancing productivity. *Energy Conversion and Management*, *49*(10): 2602–2608. DOI: https://doi.org/10.1016/j.enconman.2008.05.010

[5] Nijmeh, S., Odeh, S., & Akash, B. 2005. Experimental and theoretical study of a single-basin solar sill in Jordan. *International Communications in Heat and Mass Transfer*, *32*(3–4): 565–572. DOI: https://doi.org/10.1016/j.icheatmasstransfer.2004.06.006

[6] Manikandan, V., Shanmugasundaram, K., Shanmugan, S., Janarthanan, B., & Chandrasekaran, J. 2013. Wick type solar stills: A review. *Renewable and Sustainable Energy Reviews*, *20*: 322–335. DOI: https://doi.org/10.1016/j.rser.2012.11.046

[7] El-Sebaii, A., Aboul-Enein, S., Ramadan, M., & El-Bialy, E. 2000. Year-round performance of a modified single-basin solar still with mica plate as a suspended absorber. *Energy*, *25*(1): 35–49. DOI: https://doi.org/10.1016/s0360-5442(99)00037-7

[8] M. J. Al-Dulaimi and K. E. Amori, 2022. “Effect of receiver geometry on the optical and thermal performance of a parabolic trough collector,” Heat Transfer, 513: 2437–2457. DOI: http://doi.org/ 10.1002/htj.22406

[9] Al-Dulaimi, M. J., & Amori, K. E. 2023. A tubular solar still integrated with a heat pipe. *Heat Transfer*, *52*(4): 3353–3371. DOI: https://doi.org/10.1002/htj.22831

[10] Al-Dulaimi, M. J., & Amori, K. E. 2022. Optical and Thermal Performance of a Parabolic Trough Collector for Different Receiver Geometries. *Arabian Journal for Science and Engineering*, *47*(12): 16117–16133. DOI: https://doi.org/10.1007/s13369-022-06795-5

[11] Sharshir, S. W., Ellakany, Y. M., Algazzar, A. M., Elsheikh, A. H., Elkadeem, Edreis, E. M., Waly, A. S., Sathyamurthy, R., Panchal, H., & Elashry, M. S. 2019. A mini review of techniques used to improve the tubular solar still performance for solar water desalination. *Process Safety and Environmental Protection*, *124*: 204–212. DOI: https://doi.org/10.1016/j.psep.2019.02.020

[12] Sharshir, S. W., Eltawil, M. A., Algazzar, A. M., Sathyamurthy, R., & Kandeal, A. 2020. Performance enhancement of stepped double slope solar still by using nanoparticles and linen wicks: Energy, exergy and economic analysis. *Applied Thermal Engineering,* 174: 115278. DOI: https://doi.org/10.1016/j.applthermaleng.2020.115278

[13] H. Aghaei Zoori, F. Farshchi Tabrizi, F. Sarhaddi, F. Heshmatnezhad, 2013. Comparison between energy and exergy efficiencies in a weir type cascade solar still, Desalination 325: 113–121.

[14] Sharshir, S. W., Kandeal, A., Ismail, M., Abdelaziz, G. B., Kabeel, A., & Yang, N. 2019. Augmentation of a pyramid solar still performance using evacuated tubes and nanofluid: Experimental approach. *Applied Thermal Engineering*, *160*: 113997. DOI: https://doi.org/10.1016/j.applthermaleng.2019.113997

[15] Bouhal, T., Fertahi, S. E. D., Kousksou, T., & Jamil, A. 2018. CFD thermal energy storage enhancement of PCM filling a cylindrical cavity equipped with submerged heating sources. *Journal of Energy Storage*, *18*: 360–370. DOI: https://doi.org/10.1016/j.est.2018.05.015

[16] Agrawal, R., Singh, K. D. P., & Sharma, R. K. 2021. Experimental investigations on the phase change and thermal properties of nano enhanced binary eutectic phase change material of palmitic acid-stearic acid / CuO nanoparticles for thermal energy storage. *International Journal of Energy Research*, *46*(5): 6562–6576. DOI: https://doi.org/10.1002/er.7592

[17] Deshmukh, H., & Thombre, S. 2017. Solar distillation with single basin solar still using sensible heat storage materials. *Desalination*, *410*: 91–98. DOI: https://doi.org/10.1016/j.desal.2017.01.030

[18] Arjunan, T. V., Aybar, H. S., Sadagopan, P., Chandran, B. S., Neelakrishnan, S., & Nedunchezhian, N. 2013. The Effect of Energy Storage Materials on the Performance of a Simple Solar Still. *Energy Sources Part a Recovery Utilization and Environmental Effects*, *36*(2): 131–141. DOI: https://doi.org/10.1080/15567036.2010.493924

[19] Murugavel, K. K., Sivakumar, S., Ahamed, J. R., Chockalingam, K., & Srithar, K. 2010. Single basin double slope solar still with minimum basin depth and energy storing materials. *Applied Energy*, *87*(2): 514–523. DOI: https://doi.org/10.1016/j.apenergy.2009.07.023

[20] Agrawal, R., Singh, K. D. P., & Paswan, M. K. 2020. Review on Enhancement of Thermal Conductivity of Phase Change Materials with Nano-Particle in Engineering Applications. *Materials Today Proceedings*, *22*: 1617–1627. DOI: https://doi.org/10.1016/j.matpr.2020.02.159

[21] Suraparaju, S. K., & Natarajan, S. K. 2021. Productivity enhancement of single-slope solar still with novel bottom finned absorber basin inserted in phase change material (PCM): techno-economic and enviro-economic analysis. *Environmental Science and Pollution Research*, *28*(33), 45985–46006. DOI: https://doi.org/10.1007/s11356-021-13495-4

[22] Ghadamgahi, M., Ahmadi-Danesh-Ashtiani, H., & Delfani, S. 2020. Experimental investigation of multi-stage solar still using phase-change material. *Environmental Progress & Sustainable Energy*, *40*(1). DOI: https://doi.org/10.1002/ep.13477

[23] Grewal, R., Manchanda, H., & Kumar, M. 2023. Productivity amelioration of stepped solar still using phase change material and evacuated tube collector. *Heat Transfer*, *53*(2): 847–866. DOI: https://doi.org/10.1002/htj.22977

[24] Cheng, W. L., Huo, Y. K., & Nian, Y. L. 2019. Performance of solar still using shape-stabilized PCM: Experimental and theoretical investigation. *Desalination*, *455*: 89–99. DOI: https://doi.org/10.1016/j.desal.2019.01.007

[25] Mousa, H., Naser, J., Gujarathi, A. M., & Al-Sawafi, S. 2019. Experimental study and analysis of solar still desalination using phase change materials. *Journal of Energy Storage*, *26*: 100959. DOI: https://doi.org/10.1016/j.est.2019.100959

[26] Rufuss, D. D. W., Suganthi, L., Iniyan, S., & Davies, P. 2018. Effects of nanoparticle-enhanced phase change material (NPCM) on solar still productivity. *Journal of Cleaner Production*, *192*: 9–29. DOI: https://doi.org/10.1016/j.jclepro.2018.04.201

[27] Essa, F. A., Alawee, W. H., Mohammed, S. A., Dhahad, H. A., Abdullah, A., Alqsair, U. F., Omara, Z., & Younes, M. 2022. Improving the pyramid solar distiller performance by using pyramidal absorber, mirrors, condenser, and thermal storing material. *Case Studies in Thermal Engineering*, *40*: 102515. DOI: https://doi.org/10.1016/j.csite.2022.102515

[28] Kumar, P. M., Sudarvizhi, D., Prakash, K., Anupradeepa, A., Raj, S. B., Shanmathi, S., Sumithra, K., & Surya, S. 2021. Investigating a single slope solar still with a nano-phase change material. *Materials Today Proceedings*, *45*: 7922–7925. DOI: https://doi.org/10.1016/j.matpr.2020.12.804

[29] Saeed, M., Hachim, D., & Hameed, H. 2019. Numerical Investigation forSingle Slope Solar StillPerformance withOptimal Amount ofNano-PCM. *Journal of Advanced Research in Fluid Mechanics and Thermal Sciences*, *63*(2): 302–316.

[30] Hafs, H., Asbik, M., Boushaba, H., Koukouch, A., Zaaoumi, A., Bah, A., & Ansari, O. 2021. Numerical simulation of the performance of passive and active solar still with corrugated absorber surface as heat storage medium for sustainable solar desalination technology. *Groundwater for Sustainable Development*, *14*: 100610. DOI: https://doi.org/10.1016/j.gsd.2021.100610

[31] Moreno, S., Álvarez, C., Hinojosa, J., & Maytorena, V. 2022. Numerical analysis of a solar still with phase change material under the basin. *Journal of Energy Storage*, *55*: 105427. DOI: https://doi.org/10.1016/j.est.2022.105427

[32] Rashidi, S., Akar, S., Bovand, M., & Ellahi, R. 2018. Volume of fluid model to simulate the nanofluid flow and entropy generation in a single slope solar still. *Renewable Energy*, *115*: 400–410. DOI: https://doi.org/10.1016/j.renene.2017.08.059

[33] Khalifa, A. J. N. 2011. On the effect of cover tilt angle of the simple solar still on its productivity in different seasons and latitudes. *Energy Conversion and Management*, *52*(1): 431–436. https://doi.org/10.1016/j.enconman.2010.07.018

[34] Tanaka, H. 2009. Tilted wick solar still with external flat plate reflector: Optimum inclination of still and reflector. *Desalination*, *249*(1): 411–415. DOI: https://doi.org/10.1016/j.desal.2009.06.048

[35] Tanaka, H. 2011. Tilted wick solar still with flat plate bottom reflector. *Desalination*, *273*(2-3): 405-413. DOI: https://doi.org/10.1016/j.desal.2011.01.073

[36] Rahbar, N., & Asadi, A. 2016. Solar intensity measurement using a thermoelectric module; experimental study and mathematical

modeling. *Energy Conversion and Management*, *129*: 344–353. DOI: https://doi.org/10.1016/j.enconman.2016.10.007

[37] Holman, J. P. 2011. *Experimental Methods for Engineers*. McGraw-Hill Education.

[38] Velmurugan, V., Deenadayalan, C., Vinod, H., & Srithar, K. 2008. Desalination of effluent using fin type solar still. *Energy*, *33*(11): 1719–1727. DOI: https://doi.org/10.1016/j.energy.2008.07.001

[39] ANSYS, Inc. 2021 ANSYS Fluent Theory Guide. ANSYS Inc

[40] Rahbar, N., & Esfahani, J. 2013. Productivity estimation of a single-slope solar still: Theoretical and numerical analysis. *Energy*, *49*: 289–297. DOI: https://doi.org/10.1016/j.energy.2012.10.023